Chapter III

Heavy Metal Ion sensing and mechanisms based on nanostructured WS_2 based system

"Knowing is not enough; we must apply. Willing is not enough; we must do"

- Johann Wolfgang von Goethe

3.1 Introduction

The phrase 'heavy metals' represents metals having high atomic weight and density compared to water [1]. In practice, the phrase includes transition metals, metalloids, lanthanides, actinides, etc. [2,3]. Heavy metals are essential for several chemical reactions, biological and physiological functions. There exist several heavy metals such as Zinc (Zn), Selenium (Se), Iron (Fe), Copper (Cu), Cobalt (Co), Chromium (Cr), etc., which are essential for the proper functioning of the body [4]. Similarly, there are heavy metals such as Mercury (Hg), Cadmium (Cd), Antinomy (Sb), Arsenic (As), etc., which are non-essential [5]. Despite the essential and non-essential division of these metals, all of them are toxic above some particular limits. The technical term for this limit is 'permissible limit". Disturbingly, even at low concentrations, some of these metals are found to be toxic and responsible for different ailments. For instance, permissible limits for Hg, Cd, and As are 2, 5, and 10 ppb respectively [6,7,8]. Hg contamination may affect almost every system in the human body like cardiovascular, immune, nervous, digestive, renal, reproductive systems, etc. [9]. Similarly, Arsenic(As) contamination may cause skin, lung, bladder, liver, and prostate cancers [10]. In addition to these, essential micronutrient contaminations are also responsible for different health issues. For instance, Zn is one of the most essential trace elements and is important for memory, neuronal and learning activity. However, both the deficiency and overdose of Zn^{2+} ions can adversely affect human health. Zn deficiency can impair cognitive performance, neuropsychological behavior, attention, and other brain activities. Studies suggest that overdose of Zn can strongly impair consolidation of hippocampal-dependent memory [11–13]. Niragu mentioned the carcinogenic effects of Zn as well [14]. Although World Health Organization (WHO) has not proposed any health-based guideline value for Zn [15], according to Drinking Water Quality Standards in Japan (April 2015), the standard value of Zn intake is 1.0 mgL^{-1} [16]. However, Environmental Protection Agency (EPA) considers 0.120 mgL^{-1} of Zn as chronic [17].

Heavy metals are imperishable and present everywhere on earth in different forms. Therefore, heavy metal contamination is a natural phenomenon [18]. However, lately, anthropogenic activities have raised the counts exponentially [19]. Apparently, effective

monitoring of these heavy metal ions in the environment is a global exigency. To date, extensive research on heavy metal ion (HMI) sensing have been reported based on nano-materials [20,21]. However, the toxicity of these sensing materials limits their applicability in practical implementations [22,23]. Since TMDCs exhibit low cytotoxicity [24], investigations on TMDC-based HMI sensors have turned out to be an alternative for many researchers.

Being one of the highly exploited semiconducting TMDCs, the number of investigations regarding MoS_2-based heavy metal ion sensing is comparatively higher than that of other materials from this category. The detection of Hg ions by Jiang *et al.* might be the first attempt to use semiconducting TMDC-based FET sensors for the detection of heavy metal ions [25]. It can detect Hg, As, and Pb ions and have a Limit of Detection (LOD) of up to 0.1 ppb and a response time of 100 – 210 s [25, 26]. These sensing schemes were improved by choosing suitable flexible substrates for the deposition of MoS_2. This approach helps to obtain a flexible multiplex detector. Up to ppb level ultrafast detection (~8 s) of Cd^{2+} was realized with simultaneous monitoring of Hg^{2+} in tap water and Na^{+} in human sweat using this improvisation technique. These investigations lead to the possibilities of MoS_2 based wearable devices with the feature of multiple heavy-metal ion sensing [27]. Bare MoS_2 has also been used as a sensing material for Arsenic (As) detection in carbon microelectromechanical (C-MEMS) systems [28]. Nowadays, different nanostructures [29], heterostructure arrangements [30,31], functionalized MoS_2 [32], composites [33], and MoS_2 superstructures [34] have been introduced to sensor systems to increase their sensitivity and selectivity. On the other hand, very few studies have reported heavy metal ion sensing with WS_2. Possibly, the rise of WS_2 based heavy metal ion sensor started with fluorescence-based sensors [35-37]. These sensors are based on the fluorescence quenching properties of WS_2 nanosheets. Zuo *et al.* [35] simultaneously detected Hg^{2+} and Ag^{+} by delivering unique fluorescence intensity values at two different wavelengths in water, serum, and cell lysate samples. Using a similar principle, Ge *et al.* [36] detected Hg^{2+} in real samples. Liu *et al.* [37] enhanced the fluorescence by doping WS_2 with Boron and Nitrogen. The Boron-Nitrogen-doped WS_2 was able to detect Hg^{2+} down to 23 nM at an excitation wavelength of 280 nm. Subsequently, colorimetric sensors have also been developed [38] as Tang *et al.* [38] used the peroxidase mimic feature of WS_2 to detect lead ions of up to 4 ppb. Recently, a grain-boundary-rich polycrystalline monolayer WS_2 was also used for Hg^{2+} detection [39].

It is observed that, although there are numerous 2D material-based and non-2D material-based sensing techniques for the detection of different HMI ions, most of them deals with As^{3+}, Hg^{2+}, Cd^{2+}, and Pb^{2+} ions. Interestingly, there is rarely any report on TMDC-based detection of Zn ions. Most of the reports on Zn ion detection consider spectrometric approaches [40]. Spectroscopic techniques offer good sensitivity and selectivity along with accuracy and precision. However, spectroscopic instruments are sophisticated and demands high maintenance along with professionals to operate the same. Recently, Trachioti *et al.* attempted to detect Zn ions using graphitic electrodes functionalized with tin nanoparticles and obtained a LOD of 0.3 ppb [41]. They have used voltametric approach in this investigation. In general, these approaches require use of several reagents and expensive electrodes. In addition, to maintain the repeatability of the sensing process, optimization of several parameters is needed along with the preparation of the electrode materials [42-47].

Considering the above complexities present in the existing sensing schemes for Zn ions, we have developed a scheme for detection of Zn^{2+} ions in water based on WS_2 nanosheet/Cu electrode system. In this chapter, we have discussed the fabrication, set-up, sensing mechanism, and sensing parameters of the as-developed sensing scheme in detail. In a nutshell, WS_2 nanosheets were prepared and drop-casted onto custom-made finger-like copper (Cu) electrodes in order to fabricate a WS_2 nanosheet/Cu electrode-based sensing unit. The sensing parameters of the sensing unit were quantified by analysing and comparing the *I–V* characteristics of the bare and heavy metal ion-treated sensing unit. The fabricated system showed selectivity towards Zn^{2+} ions with a detection limit of less than 1 ppb. In this investigation, no expensive electrodes, or reagents other than WS_2 nanosheets and Cu electrodes were used.

3.2 Experimental details

3.2.1 Synthesis of WS_2 nanosheets

For the synthesis of WS_2 nanosheets, bulk WS_2 flakes were exfoliated for 3 h following the process described in *section 2.2.1*.

3.2.2 Instrumentation details

Electrical measurements were performed using a two-probe arrangement attached to a Keithley 2400© source-meter. Micrographs were obtained using SEM by JEOL, Japan. X-ray diffraction (XRD) spectra were obtained using an X-ray diffractometer (Rigaku and BRUKER AXS, Germany).

3.2.3 Fabrication of sensing unit

An electrode pattern was designed and transferred to the copper clad surface with the help of chemical transfer technique. The required pattern was fabricated on Cu clad by etching certain portion of the Cu film using iron (III) chloride ($FeCl_3$). The length of the electrode was 3.0480 cm (1.2 inch), and the width of the fingers was 0.1905 cm (0.0750 inch). The distance between two consecutive fingers was fixed as 0.1905 cm (0.0750 inches). The fabricated patterns were initially rubbed with 5000 and 7000 grit sandpapers and cleaned with acetone before carrying out further modifications. The as-synthesized WS_2 nanosheets were dispersed in double-distilled (DD) water, ultrasonicated for 20 min, and drop-casted onto the as-prepared finger-like Cu electrodes. Finally, it was dried and stored in a desiccator till further use. The fabrication process of the sensing unit is illustrated in **Fig. 3.1**.

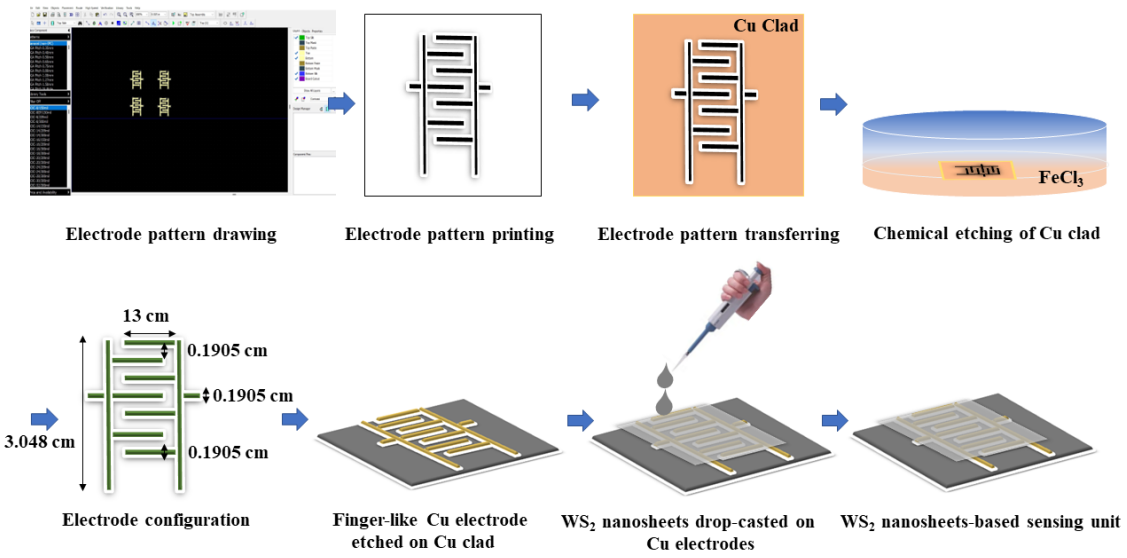

Fig.3.1. Schematic representation of the processes involved in fabrication of the sensing unit.

3.2.4 Sensor-setup and measurement techniques

The two ends of the fabricated electrodes were connected to two probes of a Keithley 2400© source-meter. A schematic of the sensing unit setup is shown in **Fig. 3.2**. The response of the sensor was determined by comparing the *I–V* characteristics of the sensing unit in presence and absence of analytes i.e. metal ions.

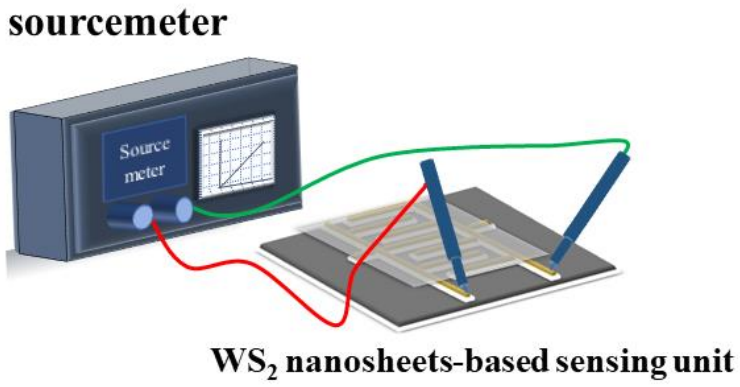

Fig.3.2. Schematic representation of the sensor set-up.

3.2.5 Preparations of standard solutions of heavy metal ions

$HgCl_2$, $NaAsO_2$, $NiCl_2$, $CuCl_2$, $SnCl_2$ and $ZnCl_2$, were purchased from Merck, and $PbCl_2$, SeO_2 were purchased from Loba Chemie®. Standard solutions of 1 ppm of these chemicals were prepared using serial dilution. Subsequently, 3, 5, 8, 9, and 10 ppb $ZnCl_2$ solutions were prepared using the same procedure.

3.3 Results and discussions

3.3.1 X-ray Diffraction (XRD)

Representative XRD spectra of the as-synthesized WS_2 nanosheets is presented in **Fig. 3.3 (a)**. The diffraction patterns of the bulk and WS_2 nanosheets followed JCPDS card no. 84–1398, indicating the hexagonal crystallographic nature of the system. By employing the Scherrer equation [48], the average crystallite size of the bulk was found to be ~ 26.37 nm and that of the nanosheets was ~19.46 nm. The reduction in crystallite size corroborates the exfoliation of WS_2.

3.3.2 Scanning Electron Microscope (SEM)

SEM image (**Fig. 3.3(b)**, scale bar– 1 μm) portrays the layered hexagonal structure of WS_2 nanostructures. The lateral dimension of the nanosheets reached up to 6.9 μm, whereas the thickness was between 80 and 100 nm.

3.3.3 Raman spectroscopy

Fig.3.3(c) shows the representative Raman Spectra of the exfoliated multilayer WS_2 nanosheets. After applying Lorentz fitting, it exhibits two prominent peaks at 345.72 cm^{-1} and 412.14 cm^{-1} corresponding to E^1_{2g} *(Γ)* and A_{1g} *(Γ)* modes respectively.

3.3.4 Electrical characterizations

Fig. 3.3(d) shows the representative *I–V* characteristics of sensor unit to be linear in the voltage range of -9 to 9 V and the maximum attained current was ~ 0.7 μA. As per

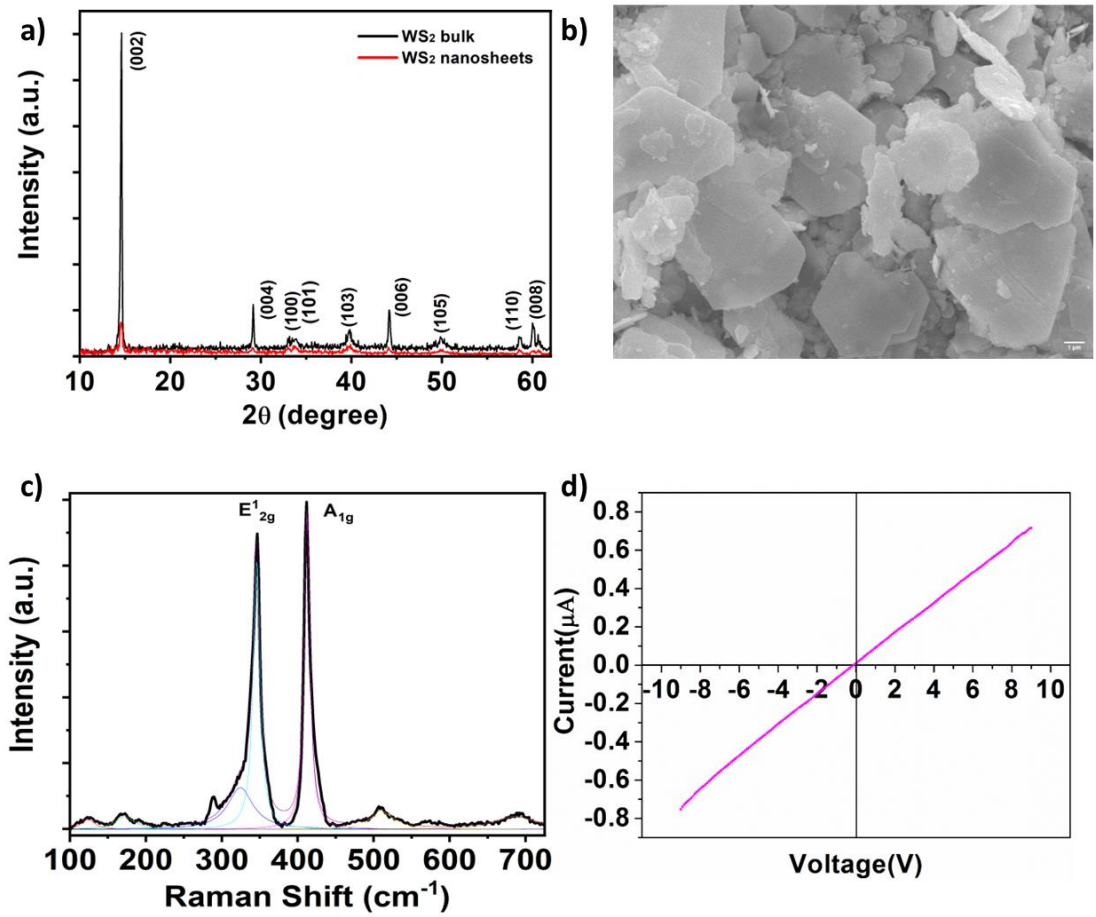

Fig.3.3. (a) XRD spectra of WS_2 bulk and nanosheets **(b)** SEM micrograph of WS_2 nanosheets **(c)** Raman spectra of WS_2 nanosheets **(d)** *I–V* characteristics of WS_2 nanosheets/Cu electrode-based sensing unit (in the absence of analytes).

published reports, WS_2 film deposited on quartz show linear characteristics [49]. Therefore, obtained results in the present work are in conformity with the earlier observations.

3.3.4.1 Effects of heavy metal ions on the *I–V* characteristic graph of the sensor unit

To investigate the effect of HMIs on the sensor unit, solutions of $HgCl_2$, $NaAsO_2$, $NiCl_2$, $CuCl_2$, $SnCl_2$, $PbCl_2$, SeO_2, and $ZnCl_2$ were prepared in DD water to introduce Hg^{2+}, As^{3+}, Ni^{2+}, Cu^{2+}, Sn^{2+}, Pb^{2+}, Se^{4+} and Zn^{2+} ions in water. Next, approximately 30 μL of each HMI solution (just a single drop) was casted onto the sensor unit and *I–V* measurements were performed for up to 20 min at intervals of 5 min. This helped us to constantly monitor the effect of the HMIs on the electrical characteristics of the unit for up to 20 min. It was apparent that, as soon as the heavy metal ions were casted on the WS_2-based unit, the current in the unit suddenly increases and the current-voltage profile experiences a deviation from the straight line.

In **Fig. 3.4(a)**, the black graph illustrates the *I-V* characteristics of the sensor unit prior to the introduction of As^{3+} ions. In this scenario, the maximum positive and negative currents were approximately +0.6 μA and -0.6 μA, corresponding to voltage values of -9 V and 9 V, respectively. Following the casting of As^{3+} ions onto the unit, all graphs, with the exception of the 20-minute graph, exhibited overlapping characteristics. The current exhibits an upward trend with an increase in potential within the positive potential region; however, the rate of increment is not uniform across the entire region. Conversely, in the negative potential region, the current diminishes as the potential decreases; however, it does not adhere to any discernible pattern. The graph associated with an interaction time of 20 minutes displayed an almost linear profile with a prominent elevation in the current values occurring between approximately 2 V and 4 V. A maximum increase in the current

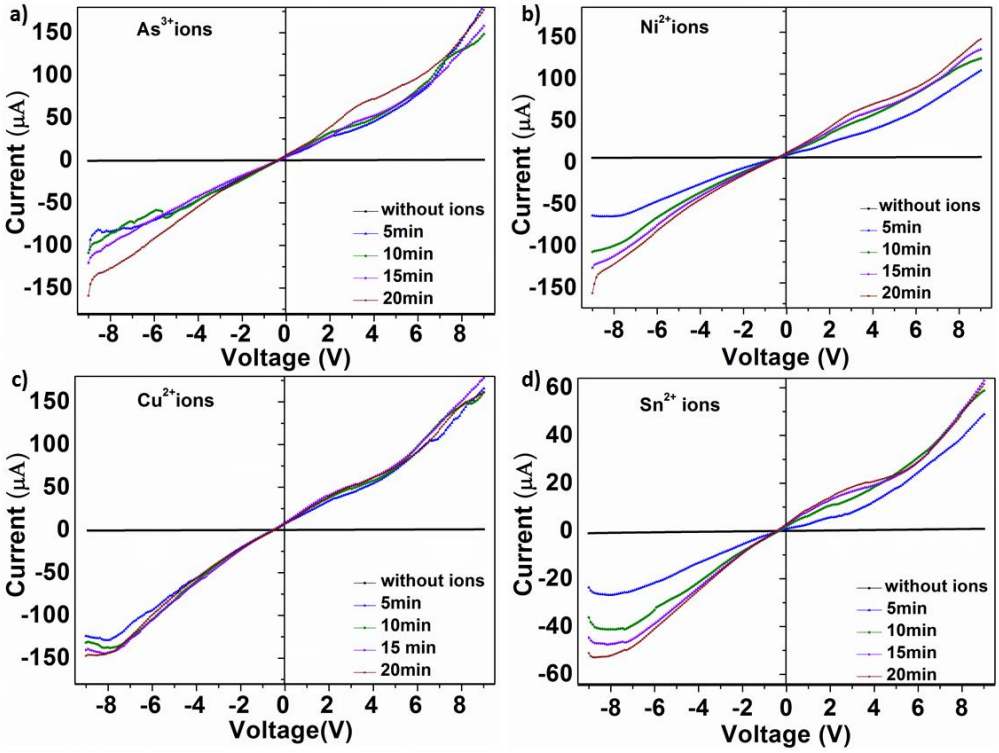

Fig.3.4. *I–V* characteristics of sensor unit treated with **(a)** As^{3+} **(b)** Ni^{2+} **(c)** Cu^{2+} and **(d)** Sn^{2+}.

of approximately 550 times was observed in the sensing unit treated with As^{3+} ions. Notably, no negative resistance region was observed in this instance.

In **Fig. 3.4(b)**, the black graph depicts the *I-V* characteristics of the sensor unit before the introduction of Ni^{2+} ions. In this scenario, the maximum positive and negative currents were determined to be approximately +0.5 μA and -0.5 μA, corresponding to voltage values of -9 V and 9 V, respectively. Upon casting Ni^{2+} ions onto the unit, an increase in current was observed with a concurrent rise in potential, followed by a polynomial trend in the positive potential region for interaction periods of 5 and 10 minutes. However, for 15 and 20 minutes, minor humps were noticeable in the graphs. In the negative potential region, the current exhibited a decreasing trend with a reduction in potential. Notably, after 5 minutes of interaction, a saturation region was identified within the range of -8 V and -9 V. The characteristic curves did not adhere to any discernible pattern. Treatment with Ni^{2+} ions resulted in an observed increment in the sensor current of approximately 300 to 350 times. Nevertheless, no negative-resistance region was evident.

In **Fig. 3.4(c)**, the graph in black represents the *I-V* characteristics of sensor unit before casting Cu^{2+} ions. The value of maximum positive current in this case were found

to be ~ 0.72 μA and negative current to be ~ 0.76 μA for the voltage values – 9 V and 9 V, respectively. After casting Cu^{2+} ions on the unit, all the characteristic graphs almost overlapped. The current linearly increases with increase in potential from 0 V to 2 V, followed by some polynomials in the positive potential region. In negative potential region, from 0 to - 8 V, current decreases with decrease in potential. However, interestingly, negative resistance regions can be observed in the negative potential region from - 8 to - 9 V. A maximum of~ 850 times increment in the current was observed for Cu^{2+} ion-treated sensor.

In **Fig. 3.4(d)**, the black graph illustrates the *I-V* characteristics of the sensor unit before the introduction of Sn^{2+} ions. In this case, the maximum positive current was found to be approximately ~0.92 μA, and the negative current was approximately ~0.97 μA for the voltage values of -9 V and 9 V, respectively. Following the casting of Sn^{2+} ions onto the unit, the current increased with an increment in potential within the positive potential region. However, the rate of increase in current was not uniform for all potential values. Notably, a negative resistance was observed in the range of -7 V to -9 V, while no negative resistance was observed in the positive potential region. A maximum increment of approximately ~150 times in the current was observed for the Sn^{2+} ion-treated sensor.

In **Fig. 3.5(a)**, the black graph illustrates the *I-V* characteristics of the sensor unit before the introduction of Se^{4+} ions. In this case, the maximum positive current was found to be +0.72 μA, and the negative current was -0.76 μA for the voltage values of -9 V and 9 V, respectively. Following the casting of Se^{4+} ions onto the unit, distinct characteristic curves were observed for all interaction times. The current exhibited an increase with an increment in applied voltage within the positive potential region; however, the rates of increase in current varied. In the negative potential region, distinct negative resistance regions were observed in the range of around -7.6 to -9 V. Notably, no negative-resistance region was observed in the positive-potential region. A maximum increment of approximately ~250 times in the current was observed for the Se^{4+} ion-treated sensing unit.

In **Fig. 3.5(b)**, the black graph illustrates the *I-V* characteristics of the sensor unit before the introduction of Hg^{2+} ions. In this case, the maximum positive current was found to be +0.26 μA, and the negative current was -0.28 μA for the voltage values of -9 V and 9 V, respectively. After the casting of Hg^{2+} ions on the unit, distinct characteristic graphs were observed. The current exhibited an increase with an increase in potential within the positive potential region. Notably, a negative-resistance region was observed in the range

of -7.6 to -9 V. Following the addition of Hg^{2+} ions, a maximum increase of approximately 260 times in the sensor's current was observed.

In **Fig. 3.5(c)**, the black graph depicts the *I-V* characteristics of the sensor unit prior to the introduction of Pb^{2+} ions. In this scenario, the maximum positive current was +0.73 μA, and the negative current was -0.73 μA for the voltage values of -9 V and 9 V, respectively. Following the casting of Pb^{2+} ions onto the unit, all characteristic graphs exhibited overlapping profiles. The current displayed an increase with an increment in potential within the positive potential region; however, the rates of increase in current varied. Notably, a small negative resistance was interestingly observed in the range of 2.2 V to 3.3 V. In the negative potential region, distinct negative resistance regions were observed in the range of -8.2 V to -9 V, excluding the graph representing the interaction for 20 minutes. A maximum increment of approximately ~350 times in the current was observed for the Pb^{2+} ion-treated sensor.

In **Fig. 3.5(d)**, the black graph illustrates the *I-V* characteristics of the sensor unit before the introduction of Zn^{2+} ions. In this case, the maximum positive current is +1 μA, and the negative current is -1 μA for the voltage values of -9 V and 9 V, respectively. Upon

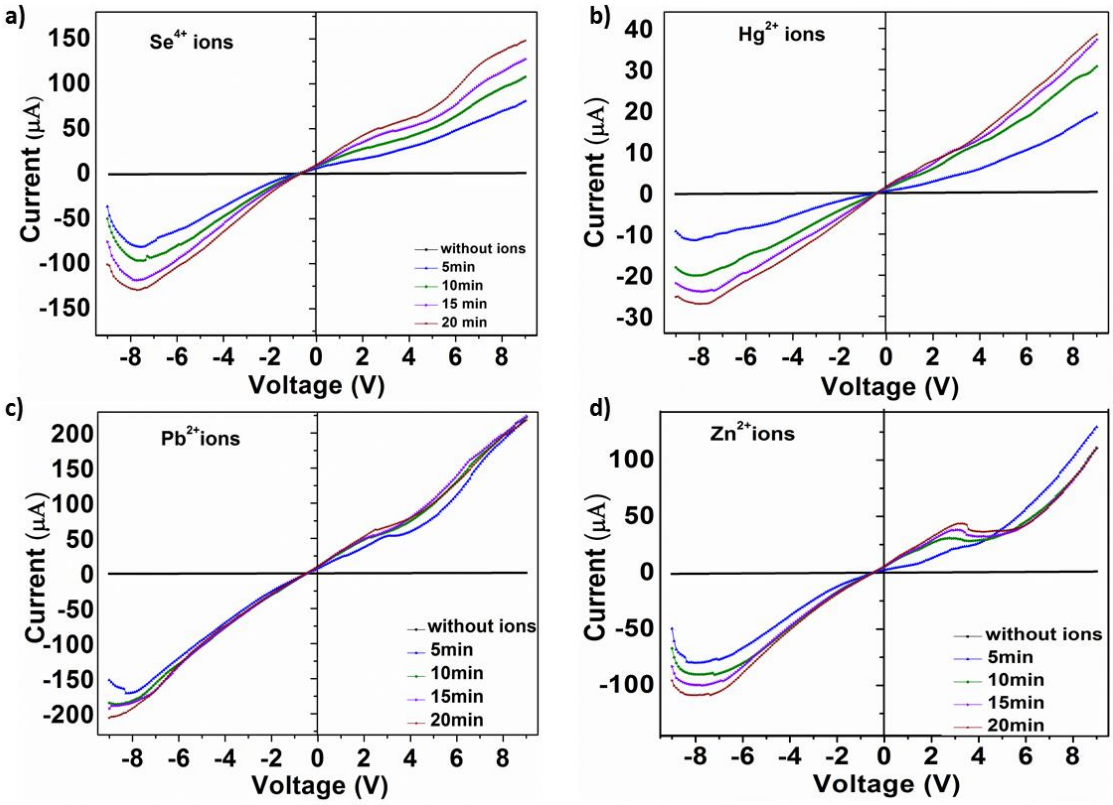

Fig.3.5. *I–V* characteristics of sensor unit treated with **(a)** Se^{4+} **(b)** Hg^{2+} **(c)** Pb^{2+} and **(d)** Zn^{2+}.

introducing Zn^{2+} ions onto the unit, the current shows an increase with a rise in applied voltage in the positive potential region. Interestingly, a distinct negative resistance region was observed in the range of 3 V to 4 V, except for the graph representing 5 minutes of interaction.

Additionally, distinct negative resistance regions were observed in the range of -7.3 V to -9 V. Remarkably, a maximum increase of approximately 800 times in the sensor's current was observed with treatment using Zn^{2+} ions.

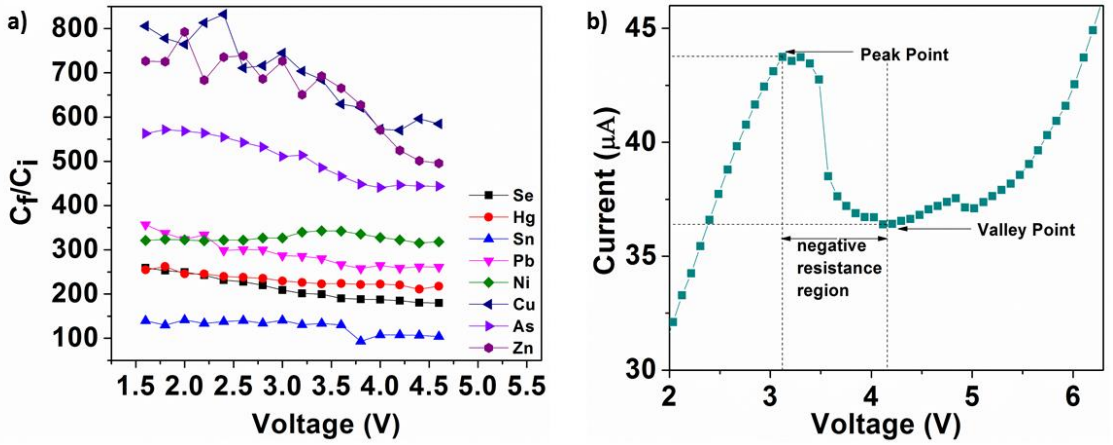

Fig.3.6. (a) Increase in current (C_f/C_i) of the sensor unit at different potential values for different heavy metal ions **(b)** *I–V* characteristics of Zn^{2+} ions showing the peak and valley point of the negative resistance region.

The increase in the current of the sensor versus the applied voltage is plotted for 8 different ions in **Fig. 3.6 (a)** for in the voltage range 1.5 V to 4.75 V. To calculate the increase in current, the ratio of the final current C_f in the circuit to the initial current C_i in the circuit was estimated at a particular voltage. The analysis showed that Zn^{2+} and Cu^{2+} resulted in the highest increase in current, while Sn^{2+} registered the lowest.

3.3.4.2 Selectivity of the proposed sensor unit

From the above *I–V* characteristics, it was observed that for some heavy metal ions, negative resistance regions in the *I–V* characteristic graphs were present, while for others, they were not. **Fig. 3.6(b)** shows the truncated version of the *I–V* characteristics of sensor unit treated with Zn^{2+} ions for 20 min. The peak and valley points in the negative potential region are clearly shown. Similarly, the peak and valley point of the Pb^{2+} ions were also obtained from the characteristic graphs and the difference between the current value at peak and valley points was calculated. **Table 3.1** compares the *I–V* characteristics of the sensor unit treated with different HMIs. From **Table 3.1**, it is evident that Zn^{2+} and Pb^{2+}

ions can be distinguished from other ions with the help of the negative resistance region present in the positive potential region of the *I–V* characteristic graphs. The values of $(i_p - i_v)$ (where $i_p$is the current at the peak point and i_v is the current at the valley point) for both ions are compared in **Table 3.2** for different interaction times. The results in **Table 3.2** imply that the maximum $(i_p - i_v)$ value for 1 ppm Pb^{2+} ions was ~13 times less than that of 1 ppm Zn^{2+} ions. Therefore, it can be perceived that the sensor is more sensitive towards Zn^{2+} ions in this regard.

Table 3.1. Comparison of *I–V* characteristics of the sensor unit treated with different HMIs.

Ions	Presence of negative resistance in the positive potential region (0 –9V)	Presence of negative resistance in the negative potential region (-9 – 0V)
As^{3+}	No	No
Ni^{2+}	No	No
Cu^{2+}	No	Yes
Sn^{2+}	No	Yes
Se^{4+}	No	Yes
Hg^{2+}	No	Yes
Pb^{2+}	Yes	Yes
Zn^{2+}	Yes	Yes

Table 3.2. $(i_p - i_v)$ for Pb^{2+} and Zn^{2+} ions for different interaction time

Ions	$(i_p - i_v)$ for 5 min (µA)	$(i_p - i_v)$ for 10 min (µA)	$(i_p - i_v)$ for 15 min (µA)	$(i_p - i_v)$ for 20 min (µA)
Pb^{2+} ions	0.29	0.56	0.45	0.3
Zn^{2+} ions	0	2.55	6	7.35

3.3.4.3 Selection of the best conditions for calibration of Zn^{2+} ions

The *I–V* characteristics of the sensor unit were obtained after casting 9 ppb Zn^{2+} ions on the sensor unit as shown in **Fig. 3.7(a)**. The difference between the peak current (i_p) and valley current (i_v), that is, $(i_p - i_v)$ at different interaction times, was calculated for 9 ppb Zn^{2+} ion treated sensor unit and plotted as shown in **Fig. 3.7(b)**. It is clear from **Fig. 3.7(b)** that the difference in the peak-to-valley current gradually increases with the increase in interaction time, thereby reaching a maximum at approximately 20 min, and then again decreases. This trend was also observed for other concentrations of Zn^{2+} ions (**Fig. A8**[£] and **Fig. A9**[ff]). Therefore, to perform further investigations, *I–V* characteristics of Zn ion treated sensor unit after 20 min of interaction were considered as the standard to compare different concentrations of Zn^{2+} ions.

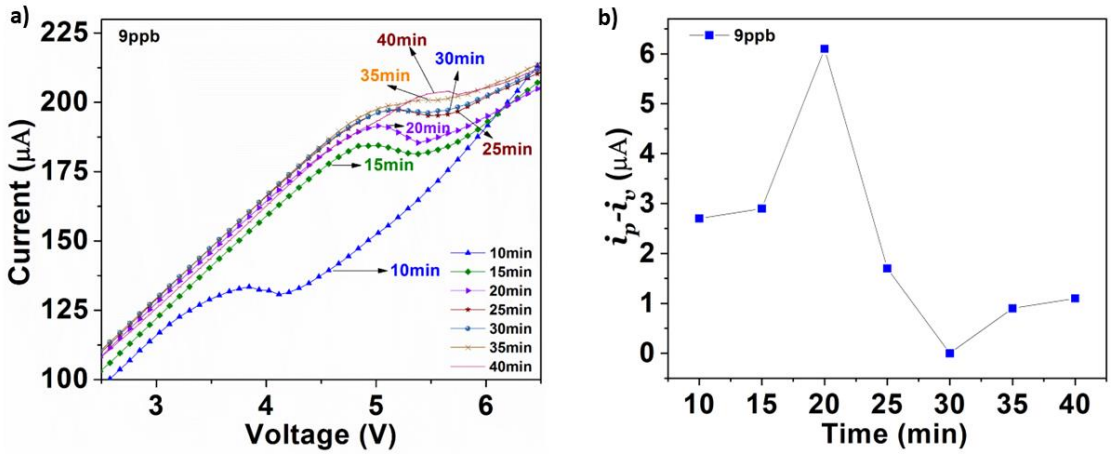

Fig.3.7. (a) *I–V* characteristics of 9 ppb Zn^{2+} ions and **(b)** $(i_p - i_v)$ at different interaction time for 9 ppb Zn^{2+} ions.

3.3.5 Limit of detection (LOD), Limit of Quantification (LOQ), sensitivity, and linear range of the proposed sensor unit

Fig. 3.8(a) shows the calibration curve for Zn^{2+}. The limit of detection (LOD) and limit of quantification (LOQ), sensitivity, and linear range of the proposed sensor were calculated from the calibration curve in **Fig. 3.8(a)** using the formulas $3\sigma/m$ and $10\sigma/m$, respectively. Here, σ is the standard deviation obtained from the regression analysis, and *m* is the slope of the linear fit. The obtained LOD and LOQ are 0.94 ± 0.05 ppb and 3.12 ± 0.05 ppb, respectively. Again, sensitivity of the sensor is 0.63 ± 0.05 μA per ppb. The linear range of the sensor is 3 to 10 ppb.

[£, ff] **Appendix**

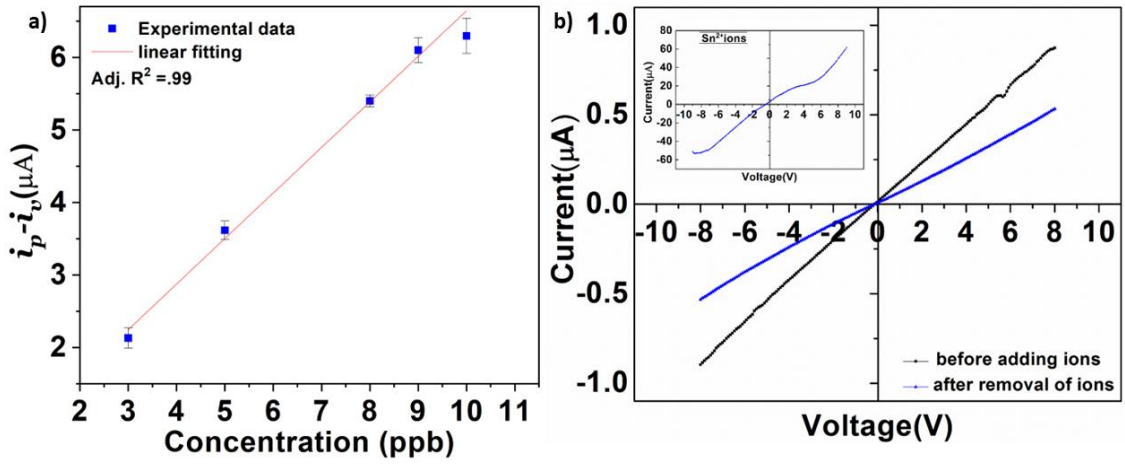

Fig.3.8. (a) Calibration curve for Zn^{2+} ions (**b)** *I–V* characteristics of the sensor before adding Sn^{2+} ions, during treatment with Sn^{2+} ions (in the inset) and after removal of Sn^{2+} ions.

3.3.6 Reversibility and repeatability

The scheme shows reversibility, as is evident from the characteristics shown in **Fig. 3.8(b)**. Prior to addition of any analytes, the *I–V* graph was linear having maximum current ~ 0.1 μA, labelled as 'before adding ions' in the **Fig 3.8(b)**. After treatment with ions (1 ppm Sn^{2+}), the current increased to ~ 60 μA (as shown in the inset). As soon as the ions were removed, the layered WS_2 system regained its linear characteristics (labelled as 'after removal of ions' in **Fig. 3.8(b)**. Similar characteristics have also been observed for all other analytes. Repeatability was tested for two concentrations 5 ppb and 1 ppm of Zn^{2+} ions **(Fig. A10**[℃] and **Fig. A11**[₦]**)**. The relative standard deviations (RSD) of 5 successive measurements of 5 ppb, and 1 ppm Zn^{2+} solution after 43 days was found to be 1.38 % and 0.27%. The lower error in $(i_p - i_v)$ in the case of 1 ppm compared to 5 ppb may be due to the high concentration of Zn^{2+} ions in this case.

3.3.7 Interference study

To check the specificity of the unit for the mixture of ions, analysis was carried out with mixtures of $Zn^{2+}$and Se^{4+}, Zn^{2+} and Hg^{2+}, Se^{4+} and Hg^{2+}, and Zn^{2+}, Se^{4+}, and Hg^{2+} ions. These two ions *viz.* Hg^{2+} and Se^{4+} were selected for the interference study because they cause systematic variation in the *I–V* characteristics with increasing interaction time with sensor units similar to Zn^{2+} ions, as evident from **Fig. 3.5(a)** and **Fig. 3.5 (b)**.

[℃, ₦]**Appendix**

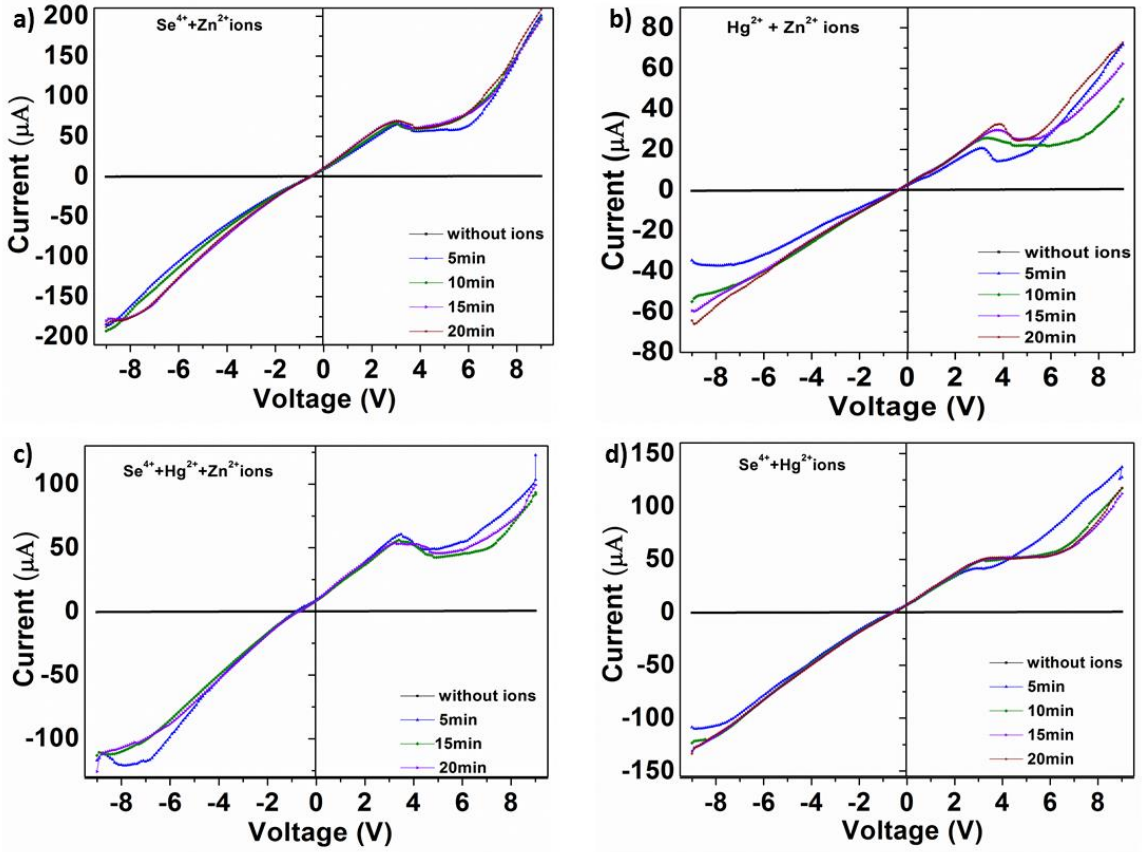

Fig.3.9. *I–V* characteristics of mixture of **(a)** $Zn^{2+}$and Se^{4+} **(b)** Zn^{2+} and Hg^{2+} **(c)** Zn^{2+}, Se^{4+} and Hg^{2+} and finally **(d)** Se^{4+} and Hg^{2+}ions.

Table 3.3. $(i_p - i_v)$ for Zn^{2+} and interfering ions

Ion/ ion mixtures	$(i_p - i_v)$ (μA) for 20 min
Zn^{2+}	~7.35
Se^{4+} + Zn^{2+}	~ 8.64
Hg^{2+}+ Zn^{2+}	~ 8.1
Se^{4+}+ Hg^{2+}+ Zn^{2+}	~ 8.1
Se^{4+}+ Hg^{2+}	~1.53

Figs. 3.9(a)–(d) show the *I–V* characteristics of the sensor treated with interfering ions. All ion mixtures produced distinct negative regions in the positive potential region, except for the Se^{4+} and Hg^{2+} mixtures. Again, in the negative potential region, a prominent negative resistance was observed only for the Se^{4+}, Hg^{2+}, and Zn^{2+} mixture after 5 min of interaction. **Table 3.3** shows the difference between the peaks and valley current for interfering ions at a concentration of 1 ppm. It was calculated that $(i_p - i_v)$ value for ions without Zn^{2+} (i.e., for Se^{4+} + Hg^{2+}) is only 1.53 μA, which is less than the value, i.e., 2.13

μA as obtained for 3 ppb Zn^{2+} ions. For other interfering ions, the value of $(i_p - i_v)$ was higher than that obtained for 1 ppm of Zn^{2+} ions (that is, 7.35 μA). Therefore, the sensor sets a clear range of $(i_p - i_v)$ for the ions without Zn^{2+} (<2 μA for 1 ppm of Hg^{2+}, As^{3+}, Ni^{2+}, Cu^{2+}, Sn^{2+}, Pb^{2+},Se^{4+}, and a mixture of Se^{4+} + Hg^{2+} ions), only Zn^{2+} ions (from 2.13 μA − 7.35 μA corresponding to concentrations from 3 ppb to 1000 ppb), and Zn^{2+} mixture with other ions (>8 μA for a mixture of Zn^{2+} and Se^{4+}; Zn^{2+} and Hg^{2+}; and Zn^{2+}, Se^{4+}, and Hg^{2+} ions). All these indicates the future of this unit in analyzing real samples.

3.3.8 Principle of sensing

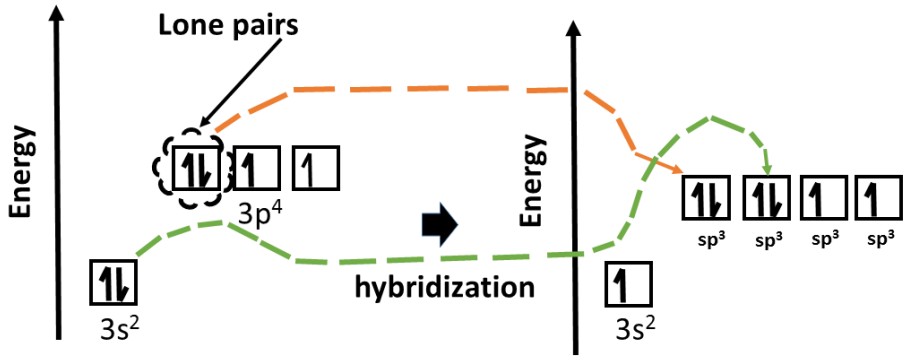

Fig.3.10. (a) energy representation of valence electrons of Sulfur (S) **(b)** electronic states of S after hybridization.

The increase in the current in the sensor due to the addition of metal ions is a result of charge transfer. There are two possible primary means through which charge transfer can occur in the present case. The first is ligand-to-metal charge transfer, where the ligand is WS_2 and the metals are heavy-metal ions. The other mechanism is the oxidation of WS_2 in the presence of a solution containing metal ions. The electronic configuration of sulfur is $1s^2 2s^2 2p^6 3s^2 3p^4$, where $1s^2 2s^2 2p^6$ and $3s^2 3p^4$ represent the inner and valence electrons respectively. The energy representation of valence electrons is shown in **Fig. 3.10(a)**. Here, one lone pair (LP) of electrons exists in the first *p* orbital. In transition metal chalcogenides, chalcogens are sp^3 hybridized [50]. The electronic states after hybridization are shown in **Fig. 3.10(b)**. In the case of WS_2, tungsten atoms are six-fold coordinated with sulfur atoms in a trigonal prismatic molecular bonding geometry. The metal atom provides four electrons to fill the bonding states. On the other hand, chalcogen provides two sp^3 hybridized unpaired electrons and one lone pair for bonding, as shown in **Fig. 3.10(b)**. Thus, transition metal and chalcogen can be ascribed to a formal charge of +4 and – 2,

respectively [51]. The Charge Density Difference (CDD) isosurfaces [50] obtained from DFT simulations demonstrate that LP electrons point into the van der Waals (vdW) gap and terminate at the surface. Therefore, when heavy metal ions are drop-casted on WS_2 nanosheets, the surface of the nanostructure acts as a Lewis base (due to the presence of lone pairs), and the metal ions act as Lewis acid initiating Lewis acid base complexes of the form $[A^{m+}{}_n(WS_2)]B^-{}_{mn}$ where A is the metal ion with an oxidation number m, B is the anion associated with AB salt, and n is the stoichiometry. The formation of the complex increases the current in the system, as reported in [52] for several Lewis-acid-base complexes. In general, any 2D semiconductor material system has very high contact resistance with a 3D metal surface [53]. Therefore, the current flow was very low in the untreated sensing unit. However, after coordination with any Lewis acid, the Fermi level moved downwards, and there was a decrease in contact resistance and channel sheet resistance, accompanied by a considerable increase in current. This behavior is dependent on the strength of the Lewis acids. Lewis acid strength depends on both the electronegativity as well as the ionic radius of the ions. A higher electronegativity and smaller ionic radius yield a higher increase in the current and vice versa. In the present case, the ions used in the investigation can be arranged in the increasing order of electronegativity as Hg<Pb<Sn<Ni<Zn<Cu<As<Se. It is obtained from the spin-polarized non-transition state Xα calculation [54]. Similarly, the ions used in the investigation can be arranged in the increasing order of ionic radius as $Zn^{2+}<Cu^{2+}<Ni^{2+}<Sn^{4+}<Hg^{2+}<Se^{4+}<As^{3+}<Pb^{2+}$. Here, Slater's analytical form of the radial part of one electron function was used to calculate the radii [55]. From the electronegativity and radius series, it is evident that Zn^{2+} and Cu^{2+} ions have relatively smaller ionic radius and have moderate electronegativity. Therefore, according to the behavior of Lewis acid, Zn^{2+} and Cu^{2+} will show highest increase in current which was observed experimentally in **Fig. 3.6(a)**. Apart from the anticipated Lewis soft-soft interaction, it has been documented that 2D TMDC nanosheets exhibit an enhanced susceptibility to oxidation compared to their bulk counterparts [56]. This heightened susceptibility to oxidation during the interaction with heavy metal ions leads to a transformative process where 2D TMDC nanosheets facilitate the reduction of ionic metal species. The extent of reduction is contingent upon the redox potential inherent to the specific metal species involved. As a consequence of this oxidation-reduction dynamic, sulfur vacancies emerge within the 2D TMDC material system. The introduction of sulfur vacancies within the 2D material structure induces a distinctive electronic behavior, notably negative resistance in the resultant TMDC nanosheet/metal electrode device [57]. In the

current experimental setup, Zn^{2+} ions may have a higher tendency for reduction and high carrier mobility compared to other ions, leading to a prominent negative resistance region in the presence of Zn ions.

The WS_2 nanosheet/Cu electrode system, under scrutiny in the present context, has also exhibited a distinctive temporal behavior owing to the real-time interplay between the WS_2 nanosheet and heavy metal ions. Consequently, a time-dependent negative resistance phenomenon has been observed (**Fig.3.7. (b)**). Notably, the tunnelling current follows a discernible pattern, escalating to a zenith at the 20-minute mark of interaction, subsequently diminishing and again increasing after a particular interval of time. This temporal behavior can plausibly be ascribed to the redox reaction transpiring at the surface of the WS_2 nanosheets upon its contact with the aqueous solution of metal ions. During this redox reaction, W and S at the surface get oxidized, whereas metal ions get reduced resulting in generation of Sulfur vacancies in the WS_2 nanosheet. These vacancies introduce quantum/defect-induced states on the WS_2 nanosheet system. Therefore, upon the application of an appropriate voltage, the Fermi level of WS_2 nanosheet may shift towards the quantum/defect-induced states, facilitating carrier tunnelling from the Cu electrode to WS_2 nanosheets and vice versa, thereby giving rise to tunnelling current. The increase in tunnelling current discernibly correlated with the initial increase in the Sulfur vacancy with time. However, it is imperative to note that the escalation in sulfur vacancies is concomitant with an increase in tungsten oxide residuals on the material's surface. Consequently, as the duration of interaction prolongs, the accumulation of oxide residuals gradually supersedes carrier transport due to the thermionic emission over resonance tunnelling in the material system. This transformative process, shifting the material system towards a classical paradigm, is correlated with the gradual decrease in tunnelling current observed post the 20-minute mark of interaction time. As the temporal evolution of the interaction unfolds, it becomes evident that, over a specific duration, the aqueous solution containing metal ions effectively permeates and gains access to the interior sulfur atoms. This intricate process results in the generation of additional sulfur vacancies within the material framework. Consequently, a discernible resurgence in the tunnelling current is observed after a substantial temporal interval.

It was also observed that after removal of analytes, the sensor unit regain its linear character with current value less than the original **Fig. 3.8(b)**. This characteristic may be

attributed to detachment of the by-products such as oxides formed in the system along with the removal of the analyte after completion of the sensing process **(Fig. A12[₱])** causing decrease in career concentration in the material system as a whole.

3.3.9 Comparison with other studies

Table 3.4 shows a comparison of the present study with recent findings. It is evident that the present sensor has an excellent detection limit, repeatability, and sensitivity, albeit with scope for improvement in the linear range. Unlike other electrochemical sensors, the present sensor shows reversibility, which can be achieved simply by removing the HMIs from the sensor surface using a pipette. Therefore, the same sensing unit can be used to analyze multiple analyte samples. However, with every use, the current value of the sensor unit was reduced (**A12[₱]**). Interestingly, the analysis showed that this did not significantly affect the sensing process.

Table 3.4. Comparison of the analytical parameters of the proposed sensor with other electrochemical sensors applied for Zn detection.

Electrode	**Measurement technique**	**Limit of detection (ppb)**	**Linear range (ppb)**	**Repeatability**	**Ref**
[1] SPGE	*SWV	2.5	10 to 70	3.0% (RSD for n = 10 of 20 ppb)	**[31]**
[2]Bismuth film/N/IL/G/SPCE	**SWASV	0.09	0.1 to 100	<8.0 % (RSD for n=10 5 ppb)	**[32]**
[3]Porous-g-C3N4/ O-MWCNTs/SPE	***DPV	0.008	4.2 to 202	-----	**[33]**
[4]zincon-EG/SPE	DPV	5	250-1500	6.9 % (RSD for n=5)	**[34]**
[5]Cr-SPE	SWASV	25	80–800	≤9.34%	**[35]**
[6]Bi/AuNP-SPCE	****DPASV	0.055	1–150	0.58% (RSD for n=10, 300 ppb)	**[36]**
WS_2 nanosheet coated finger like Cu electrodes	*I–V* characteristics	0.94	1-10	1.38 % (RSD for n=5 for 5 ppb)	Present work

[1]screen-printed gold electrode, [2]bismuth film/Nafion/ionic liquid/graphene composite modified screen-printed carbon electrode, [3]porous graphitic carbon nitride nanosheets/oxidized multiwalled carbon nanotubes, [4]zincon-EG/SPE zincon and electrochemically exfoliated graphite complex modified screen-printed Electrode, [5]chromium (III) oxide modified screen-printed electrode, [6](Bi)) film and gold nanoparticles

(AuNPs) *Square-wave voltammetry, **Square wave anodic stripping voltammetry, ***differential pulse voltammetry, ****differential pulse anodic stripping voltammetric

3.4 Conclusion

This chapter focuses on the sensing techniques and attributes of WS_2 nanosheet/Cu electrode-based sensing units. Multilayered sheets of WS_2 were synthesized using the solvo-sonication method and different characterizations such as XRD, Raman, and SEM etc. were performed. The obtained nanosheets were drop-casted on finger-like Cu electrodes to fabricate the sensing units. The sensing units without analytes exhibited linear ohmic characteristics. With the addition of analytes (i.e., heavy metal ions) in the sensing unit, a maximum increase of approximately 850 times in the current was observed. This was further accompanied by a nonlinear current–voltage (*I–V*) response. The sensing performance of the unit was tested using various heavy metals. The negative-resistance region that appeared due to the introduction of analytes in the *I–V* characteristics of the sensing unit was considered as the basis for quantitative evaluation of the sensing parameters of the unit. The results show that the unit has considerable selectivity towards Zn^{2+}. Consequently, the detection limit was affixed to 0.94 ± 0.05 ppb and sensitivity to 0.63 ±0.05 µA per ppb. The repeatability of the sensing unit was ensured as some of the results were repeatable even after 43 days with a maximum deviation of 1.38%. The sensing unit is reversible in the sense that it resumes its linear characteristics after removal of the HMIs from the sensor surface. The response of the sensing unit may be due to ligand-to-metal charge transfer, where the ligand is WS_2 and the metals are heavy-metal ions; and the oxidation of WS_2 in the presence of analytes. It was impressive to realize that this simple sensing scheme triggered Zn speciation without addition of any other reagents.

References

[1] Ferguson, J.E. *The Heavy Elements: Chemistry, Environmental Impact and Health Effects*. Pergamon Press, NY 10523, 614, 1990.

[2] Singh, M.R. Impurities-heavy metals: IR perspective. *International Journal of the Physical Sciences*, 5(4): 1045-1058, 2007.

[3] Duffus, J.H. "Heavy Metals"–A Meaningless Term. *Chemistry International--News-magazine for IUPAC*, 23(6): 163-167, 2001.

[4] World Health Organization, Trace Elements in Human Nutrition and Health. Office of publications WHO, Geneva, Switzerland, 1996

[5] Chang, L.W., Magos, L. and Suzuki, T., editors, *Toxicology of Metals*. Lewis, Boca Raton, FL, 1996.

[6] Li, F., Wang, J., Lai, Y., Wu, C., Sun, S., He, Y. and Ma, H. Ultrasensitive and selective detection of copper (II) and mercury (II) ions by dye-coded silver nanoparticle-based SERS probes. *Biosensors and Bioelectronics*, 39(1): 82-87, 2013.

[7] Wang, A.J., Guo, H., Zhang, M., Zhou, D.L., Wang, R.Z. and Feng, J.J. Sensitive and selective colorimetric detection of cadmium (II) using gold nanoparticles modified with 4-amino-3-hydrazino-5-mercapto-1, 2, 4-triazole. *Microchimica Acta*, 180(11): 1051-1057, 2013.

[8] Melamed, D. Monitoring arsenic in the environment: a review of science and technologies with the potential for field measurements. *Analytica Chimica Acta*, 532(1): 1-13, 2005.

[9] Rice, K.M., Walker Jr, E.M., Wu, M., Gillette, C. and Blough, E.R. Environmental mercury and its toxic effects. *Journal of Preventive Medicine and Public Health*, 47(2): 74, 2014.

[10] Hong, Y.S., Song, K.H. and Chung, J.Y. Health effects of chronic arsenic exposure. *Journal of Preventive Medicine and Public Health*, 47(5): 245, 2014.

[11] Chen, N.N., Zhao, D.J., Sun, Y.X., Wang, D.D. and Ni, H. Long-term effects of zinc deficiency and zinc supplementation on developmental seizure-induced brain damage and the underlying GPR39/ZnT-3 and MBP expression in the hippocampus. *Frontiers in Neuroscience*, 13: 920, 2019.

[12] Contestabile, A., Peña-Altamira, E., Virgili, M. and Monti, B. Zinc supplementation in rats impairs hippocampal-dependent memory consolidation and dampens post-traumatic recollection of stressful event. *European Neuropsychopharmacology*, 26(6): 1070-1082, 2016.

[13] Hagmeyer, S., Haderspeck, J.C. and Grabrucker, A.M. Behavioral impairments in animal models for zinc deficiency. *Frontiers in Behavioral Neuroscience*, 8: 443, 2015.

[14] Nriagu, J. Zinc Toxicity in Humans. In Nriagu, J, editor, *Encyclopedia of Environmental Health*; 2nd edition, volume 1, Elsevier Publishers, 2011.

[15] World Health Organization. *Guidelines for Drinking-Water Quality: Fourth Edition Incorporating the First Addendum.* WHO, Geneva, 2017.

[16] The Ministry of Health, Labour and Welfare of Japan, *Drinking Quality Standards*. Retrieved on 20th Dec. 2022 from https://www.mhlw.go.jp/english/policy/health/water_supply/dl/4a.pdf, 2015.

[17] EPA, *National Recommended Water Quality Criteria—Aquatic Life Criteria Table*. Retrieved on 23rd Dec. 2022 from https://www.epa.gov/wqc/national-recommended-water-quali ty-criteria-aquatic-life-criteria-table, last updated on 15th Sep. 2022.

[18] Nriagu, J.O., A global assessment of natural sources of atmospheric trace metals. *Nature*, 338(6210): 47-49, 1989.

[19] Goyer, R.A. and Clarkson, T.W. Toxic effects of metals. *Casarett and Doull's Toxicology: The Basic Science of Poisons*, 5: 691-736, 1996.

[20] Boruah, B. S. Detection of Hazardous Heavy Metal Ions In Water Through Optical and Electrical Methods and Their Comparative Sensitivity Analysis. Department Of Physics, Tezpur University, India, 2020.

[21] RAJ, S. I. Green Synthesis of Metal Sulfide/Oxide Nanomaterials and its Application in Heavy Metal Ion Sensing and Removal of Dyes. Department of Chemistry, Indira Gandhi National Tribal University, Amarkantak, M.P., 484887, 2020.

[22] Attarilar, S., Yang, J., Ebrahimi, M., Wang, Q., Liu, J., Tang, Y. and Yang, J. The toxicity phenomenon and the related occurrence in metal and metal oxide nanoparticles: a brief review from the biomedical perspective. *Frontiers in Bioengineering and Biotechnology*, 8: 822, 2020.

[23] Długosz, O., Szostak, K., Staroń, A., Pulit-Prociak, J. and Banach, M. Methods for reducing the toxicity of metal and metal oxide NPs as biomedicine. *Materials*, 13(2): 279, 2020.

[24] Appel, J.H., Li, D.O., Podlevsky, J.D., Debnath, A., Green, A.A., Wang, Q.H. and Chae, J. Low cytotoxicity and genotoxicity of two-dimensional MoS_2 and WS_2. *ACS Biomaterials Science & Engineering*, 2(3): 361-367, 2016.

[25] Jiang, S., Cheng, R., Ng, R., Huang, Y. and Duan, X. Highly sensitive detection of mercury (II) ions with few-layer molybdenum disulfide. *Nano Research*, 8(1): 257-262, 2015.

[26] Li, P., Zhang, D., Sun, Y.E., Chang, H., Liu, J. and Yin, N., Towards intrinsic MoS_2 devices for high performance arsenite sensing. *Applied Physics Letters*, 109(6): 063110, 2016.

[27] Li, P., Zhang, D. and Wu, Z. Flexible MoS_2 sensor arrays for high performance label-free ion sensing. *Sensors and Actuators A: Physical*, 286: 51-58, 2019.

[28] Majumder, S., Pramanick, B., Mondal, M. and Bhattacharyya, T.K. Carbon Electrodes for Low Power Heavy Metal Sensing Using MoS_2 Based Resistive Sensors. In *IEEE SENSORS* ,1-4, New Delhi, October, 2018.

[29] Hwang, J.H., Islam, M.A., Choi, H., Ko, T.J., Rodriguez, K.L., Chung, H.S., Jung, Y. and Lee, W.H. Improving electrochemical Pb^{2+} detection using a vertically aligned 2D MoS_2 nanofilm. *Analytical Chemistry*, 91(18): 11770-11777, 2019.

[30] Mohammadi, A., Heydari-Bafrooei, E., Foroughi, M.M. and Mohammadi, M. Heterostructured Au/MoS_2-MWCNT nanoflowers: A highly efficient support for the electrochemical aptasensing of solvated mercuric ion. *Microchemical Journal*, 158: 105154, 2020.

[31] Nigam, A., Goel, N., Bhat, T.N., Rahman, M.T., Dolmanan, S.B., Qiao, Q., Tripathy, S. and Kumar, M. Real time detection of Hg2+ ions using MoS_2 functionalized AlGaN/GaN high electron mobility transistor for water quality monitoring. *Sensors and Actuators B: Chemical*, 309: 127832, 2020.

[32] Bazylewski, P., Van Middelkoop, S., Divigalpitiya, R. and Fanchini, G. Solid-state chemiresistors from two-dimensional MoS_2 nanosheets functionalized with l-Cysteine for In-line sensing of Part-Per-Billion Cd^{2+} ions in drinking water. *ACS Omega*, 5(1): 643-649, 2019.

[33] Sun, Y.F., Sun, J.H., Wang, J., Pi, Z.X., Wang, L.C., Yang, M. and Huang, X.J. Sensitive and anti-interference stripping voltammetry analysis of Pb (II) in water using flower-like MoS_2/rGO composite with ultra-thin nanosheets. *Analytica Chimica Acta*, 1063: 64-74, 2019.

[34] Xue, T., Qi, K. and Hu, C. Novel SPR sensing platform based on superstructure MoS_2 nanosheets for ultrasensitive detection of mercury ion. *Sensors and Actuators B: Chemical*, 284: 589-594, 2019.

[35] Zuo, X., Zhang, H., Zhu, Q., Wang, W., Feng, J. and Chen, X. A dual-color fluorescent biosensing platform based on WS_2 nanosheet for detection of Hg^{2+} and Ag^{+}. *Biosensors and Bioelectronics*, 85: 464-470, 2016.

[36] Ge, J., Geng, X., Du, Y., Chen, J., Zhang, L., Bai, D.M., Ji, D.Y., Hu, Y.L., Li, Z.H. Highly sensitive fluorescence detection of mercury (II) ions based on WS_2 nanosheets and T7 exonuclease assisted cyclic enzymatic amplification *Sensors and Actuators B: Chemical*, 249: 189-194, 2017.

[37] Feng, B., Liu, X., Zheng, Y., Xiao, Q., Wu, N. and Wang, S. A label-free fluorescent probe for Hg^{2+} based on boron-and nitrogen-doped photoluminescent WS_2. *RSC Advances*, 6(55): 49668-49674, 2016.

[38] Tang, Y., Hu, Y., Yang, Y., Liu, B. and Wu, Y. A facile colorimetric sensor for ultrasensitive and selective detection of Lead (II) in environmental and biological samples based on intrinsic peroxidase-mimic activity of WS_2 nanosheets. *Analytica Chimica Acta*, 1106: 115-125, 2020.

[39] Liu, L., Ye, K., Lin, C., Jia, Z., Xue, T., Nie, A., Cheng, Y., Xiang, J., Mu, C., Wang, B. and Wen, F. Grain-boundary-rich polycrystalline monolayer WS_2 film for attomolar-level Hg^{2+} sensors. *Nature Communications*, 12(1): 1-8, 2021.

[40] Wang, Z., Wang, X., Wang, Q., Xiong, X., Luo, H. and Huang, K. Recent developments in chemical vapor generation atomic spectrometry for zinc detection. *Microchemical Journal*, 149: 104052, 2019.

[41] Trachioti, M.G., Hrbac, J. and Prodromidis, M.I. Determination of Cd and Zn with "green" screen-printed electrodes modified with instantly prepared sparked tin nanoparticles. *Sensors and Actuators B: Chemical*, 260: 1076-1083, 2018.

[42] da Silva, S.M., Squissato, A.L., Rocha, D.P., Vasconcellos, M.L., de Q Ferreira, R., Richter, E.M. and Munoz, R.A. Improved anodic stripping voltammetric detection of zinc on a disposable screen-printed gold electrode. *Ionics*, 26(5): 2611-2621, 2020.

[43] Chaiyo, S., Mehmeti, E., Žagar, K., Siangproh, W., Chailapakul, O. and Kalcher, K. Electrochemical sensors for the simultaneous determination of zinc, cadmium and lead using a Nafion/ionic liquid/graphene composite modified screen-printed carbon electrode. *Analytica Chimica Acta*, 918: 26-34, 2016.

[44] Ramalingam, M., Ponnusamy, V.K. and Sangilimuthu, S.N., A nanocomposite consisting of porous graphitic carbon nitride nanosheets and oxidized multiwalled carbon nanotubes for simultaneous stripping voltammetric determination of cadmium (II), mercury (II), lead (II) and zinc (II). *Microchimica Acta*, 186(2): 1-10, 2019.

[45] Teng, Y., Singh, C.K., Sadak, O., Ahmad, N. and Gunasekaran, S. Electrochemical detection of mobile zinc ions for early diagnosis of prostate cancer. *Journal of Electroanalytical Chemistry*, 833: 269-274, 2019.

[46] Koudelkova, Z., Syrovy, T., Ambrozova, P., Moravec, Z., Kubac, L., Hynek, D., Richtera, L. and Adam, V. Determination of zinc, cadmium, lead, copper and silver using a carbon paste electrode and a screen printed electrode modified with chromium (III) oxide. *Sensors*, 17(8): 1832, 2017.

[47] Lu, Z., Zhang, J., Dai, W., Lin, X., Ye, J. and Ye, J. A screen-printed carbon electrode modified with a bismuth film and gold nanoparticles for simultaneous stripping voltammetric determination of Zn (II), Pb (II) and Cu (II). *Microchimica Acta*, 184(12): 4731-4740, 2017.

[48] Jenkins R, Snyder RL. *Introduction to X-ray Powder Diffractometry*. John Wiley & Sons, NY, volume 138, 1996.

[49] Perea-López, N., Elías, A.L., Berkdemir, A., Castro-Beltran, A. Gutiérrez, H.R., Feng, S., Lv, R., Hayashi, T., López-Urías, F., Ghosh, S. and Muchharla, B. Photosensor device based on few-layered WS_2 films. *Advanced Functional Materials*, 23(44): 5511-5517, 2013.

[50] Kolobov, A.V. and Tominaga, J. *Two Dimensional Transition-Metal Dichalcogenides*. Springer International Publishing, Switzerland, volume 239, 2016.

[51] Chhowalla, M., Shin, H.S., Eda, G., Li, L.J., Loh, K.P. and Zhang, H. The chemistry of two-dimensional layered transition metal dichalcogenide nanosheets. *Nature Chemistry*, 5(4): 263-275, 2013.

[52] Lei, S., Wang, X., Li, B., Kang, J., He, Y., George, A., Ge, L., Gong, Y., Dong, P., Jin, Z. and Brunetto, G. Surface functionalization of two-dimensional metal chalcogenides by Lewis acid–base chemistry. *Nature Nanotechnology*, 11(5): 465-471, 2016.

[53] Allain, A., Kang, J., Banerjee, K. and Kis, A. Electrical contacts to two-dimensional semiconductors. *Nature Materials*, 14(12): 1195-1205, 2015.

[54] Sen, K.D. and Jørgensen, C.K., editors, *Electronegativity*. Springer, Berlin Heidelberg, 27-40, 1987.

[55] Ghosh, D.C. and Biswas, R. Theoretical calculation of absolute radii of atoms and ions. Part 2. The ionic radii. *International Journal of Molecular Sciences*, 4(6): 379-407, 2003.

[56] Wang, Z., Sim, A., Urban, J.J. and Mi, B. Removal and recovery of heavy metal ions by two-dimensional MoS_2 nanosheets: performance and mechanisms. *Environmental science & technology*, 52(17): 9741-9748, 2018.

[57] Chang, W.H., Lu, C.I., Yang, T.H., Yang, S.T., Simbulan, K.B., Lin, C.P., Hsieh, S.H., Chen, J.H., Li, K.S., Chen, C.H. and Hou, T.H. Defect-engineered room temperature

negative differential resistance in monolayer MoS_2 transistors. *Nanoscale Horizons*, 7(12): 1533-1539, 2022.